Characterisation of damage mechanisms of GFRP-balsa sandwich under 4-point bending based on two-step clustering process in acoustic emission analysis

Yuan Wu, Marie-Laetitia Pastor, Marianne Perrin, Pascal Casari, Xiaojing Gong

Characterisation of damage mechanisms of GFRP-balsa sandwich under 4-point bending based on two-step clustering process in acoustic emission analysis

Yuan Wu
Institut Clément Ader (ICA), CNRS, UMR 5312, University of Toulouse, UPS, 1 rue Lautréamont, 65000, Tarbes, France
Institut de Recherche en Génie Civil et Mécanique, GeM-E3M, CNRS, UMR 6183, University of Nantes, 58 rue Michel Ange, 44600, Saint-Nazaire, France

Marie-Laetitia Pastor, Marianne Perrin
Institut Clément Ader (ICA), CNRS, UMR 5312, University of Toulouse, UPS, 1 rue Lautréamont, 65000, Tarbes, France

Pascal Casari
Institut de Recherche en Génie Civil et Mécanique, GeM-E3M, CNRS, UMR 6183, University of Nantes, 58 rue Michel Ange, 44600, Saint-Nazaire, France

Xiaojing Gong
Institut Clément Ader (ICA), CNRS, UMR 5312, University of Toulouse, UPS, 1 rue Lautréamont, 65000, Tarbes, France

This work focuses on the characterisation of damage mechanisms of GFRP-balsa sandwich under static 4-point bending by coupling Acoustic Emission (AE) monitoring and post-mortem microscope observations. A two- step clustering process coupling the three most relevant AE parameters (amplitude, peak frequency and dura-tion) has been proposed and validated to better apply the K-means method to AE analysis of damage mechanisms of the complex GFRP-balsa sandwich. It verifies that cumulative counts can be the very meaningful AE indicator for the identification of initiation of microscopic and macroscopic damages in glass/epoxy composite skins. The importance of peak frequency and duration distributions has been emphasized to better identify balsa core damages and skin/core debonding. It is interesting to find that balsa wood can release signals with peak fre-quency higher than 200 kHz and amplitude lower than 60 dB even though there is no visible core damage by microscopic observations. Finally, it concludes that damage mechanisms of GFRP-balsa sandwich under 4-point bending could occur in balsa core: balsa/balsa interfacial debonding between small balsa blocks and micro-cracking in balsa core; at the interface between composite skin and balsa core; in the composite skin: matrix cracking, fiber/matrix debonding, delamination and fiber breakage. The correlations between these damage mechanisms and characteristics of the selected three AE parameters are also proposed.

1. Introduction

Recently, composite sandwich structures consisting of thin Fiber Reinforced Polymer (FRP) laminate skins and thicker balsa wood core [1,2] have become more and more popular in civil infrastructure, wind turbine blades, marine, aircraft and aerospace applications, due to their higher specific stiffness/strength and environment friendly properties. Balsa wood is a renewable resource with low energy consumption that reduces the emission of CO_2 during the whole life cycle, and it is one of the low-density and fast-growing wood species [3], making it one of the preferred core materials in sandwich structures [4]. However, the complex behaviors of balsa wood, including the strong anisotropy [3], heterogeneity, sensitivity to humidity [1,4] and temperature, increase the difficulty to characterise its damage mechanisms. Furthermore, when balsa is bonded to FRP laminates, the mechanical behaviors and damage accumulation process could become much more complicated [5–8]. The composite sandwich structures are often subjected to bending loads, the skins are loaded under traction and compression, while the core mainly carries shear stress. In such cases, more than three damage mechanisms may appear simultaneously, such as balsa core damages, skin/core debonding, and laminated skin damages [5–8]. So, it is very difficult to clearly identify when, where and which kinds of damage mechanisms will be initiated and expanded in balsa sandwich structures, and how these different damage modes will affect the properties of the whole sandwich structure. In fact, only very few authors [6–8] have pointed out the damage mechanisms of balsa sandwich structures, and their conclusions have been drawn mainly from the traditional post-mortem observations of fracture surfaces. For example, Zaharia S M et al. [6] have studied the static and fatigue behavior of carbon-fiber-reinforced polymer (CFRP)-balsa sandwich under 3-point loading, concluding that skin/core debonding firstly occurred at the upper skin (compressive side) of the sandwich, followed by the shear crack of the entire balsa core and eventually by the debonding of the lower skin/core interface (tensive side). Based on the microscopic observations and digital image correlation (DIC), Sayahlatifi S et al. [7] and Shi H et al. [8] have found that the damage sequences of aluminum-balsa sandwich and glass-fiber-reinforced polymer (GFRP)-balsa sandwich under 3-point and 4-point bending were firstly balsa core shear cracks and then skin/core debonding, while the two skins remained undamaged. Indeed, damage mechanisms of sandwich structures may depend on many different variables [8,9], such as the loading condition, thicknesses, densities and material properties of the skin and the core, the bonding quality of the skin/core interfaces as well as the environmental parameters. Thus, the existing literatures about damage characterisation of the sandwich structures having balsa core and composite skin should be enriched to evaluate the mechanical performance of such complex wood-laminate composite materials. Accordingly, it is necessary to introduce some Non-Destructive Testing (NDT) techniques [10,11] to help monitor the damage initiation and evolution process of the balsa cored composite sandwich structures.

In the past decades, the rapid development of NDT techniques has opened up new opportunities for us to have a better understanding of the complex microscopic damage mechanisms of composite structures. Among most common NDT techniques, Acoustic Emission (AE) is preferred because it can achieve the in-situ monitoring in real time [12] by identifying the damage evolution process [13], classifying the damage modes [14,15] and localizing the damages [16,17]. AE is based on the transmission of stress wave generated by a growing internal damage

source under loading [11], such as crack initiation and propagation. A huge number of acoustic signals will be generated during mechanical tests. Consequently, one of the most challenging aspects of the application of AE technique to the monitoring of damage modes of a composite material is the analysis of the stochastic data [18–22]. At present, compared to the waveform analysis from frequency-domain, for example, the use of wavelet entropy [19] as a signal discriminator and a damage index, the parametric analysis [20–22] of AE signals is more popular due to the quicker data recording and processing. Only several most important AE parameters will be processed in time or frequency domain. It has been proven that amplitude, counts, duration, energy, rise time and peak frequency [20–22] are the most useful parameters to distinguish different damage mechanisms of composite laminates. However, the characteristics of these parameters could depend on the sensor types, loading condition, material properties and geometry of the structure etc. Recently, Unsupervised Pattern Recognition (UPR) [12–15] methods such as K-means algorithm have been mostly widely used to classify signals into different clusters when the expected cluster number is unknown. Some authors have also proposed new methods to classify damages of composites. For example, Friedrich et al. [23] have explored several indices, called c value, to perform the signal separation of damage process in glass-fiber-reinforced polymer (GFRP) plates, based on amplitude and low frequency distributions. The value c is the slope of the curve that links the distribution of hits as a function of the frequency. Barile et al. [24] have realized the AE feature selection based on Laplacian scores, and then chosen amplitude, frequency and entropy to classify damage modes of carbon-fiber-reinforced polymer (CFRP) composites. Some authors have also combined new parameters like Lempel-Ziv (LZ) complexity [25] with peak amplitude of the acoustic signal and its weighted peak frequency to distinguish different damage modes of plain weave fabric CFRP laminates. Eventually, most of them have demonstrated that the damage sequence of composite laminates could be matrix cracking, fiber/matrix debonding, delamination and fiber breakage in most tensile [10,26] and bending [12] tests, based mainly on the clustering of amplitude and frequency lower than 400 kHz. In summary, for the characterisation of CFRP/GFRP laminate skin damages, amplitude and frequency could be the most important AE descriptors.

However, concerning the correlation between the AE signals and the damage modes of the heterogeneous composite sandwich structures composed of CFRP/GFRP skin and wood/foam/honeycomb core, only very few researches mainly focusing on amplitude distributions can be found, as concluded in Table 1 [9,12,27–30]. Table 1 groups AE parameters used to assess damage mechanisms in composite sandwiches in existing literatures. In Table 1, Quispitupa A et al. [27] have studied tensile characteristics of CFRP-honeycomb sandwiches under static and fatigue loadings. Based on the clustering of AE amplitude, they have concluded that the predominant damage modes were the core damages, followed by skin/core interfacial debonding, resin cracking and fiber rupture. Fotouhi M et al. [13] and Pashmforoush F et al. [28] have demonstrated that frequency domain analysis can be an efficient tool for the identification of different damages mechanisms of woven GFRP-foam sandwiches in Double Cantilever Beam (DCB) tests. They found that foam core failure was followed by interfacial adhesive debonding, matrix cracking and fiber breakage. Tabrizi I E et al. [29] have determined the failure sequence and damage classification of GFRP-honeycomb sandwiches under 3-point bending by clustering peak frequency and duration. They concluded that the major damages initiate as core failure, followed by skin/core debonding, matrix cracking and fiber breakage. Masmoudi S et al. [12] have compared AE amplitude and waveforms to classify different damage mechanisms of E-glass-fiber-PVC foam sandwiches under 3-point bending. They verified that foam core damage was the most dominant, followed by resin cracking, interfacial debonding and fiber breakage. However, based on the clustering of AE amplitude, Assarar et al. [30] have reported that matrix cracking of E-glass-fiber-PVC foam sandwiches appeared firstly and presented 80% of the total damages, and then followed by fiber/matrix debonding (40–75 dB), skin/core debonding, skin delamination (50–85 dB) and fiber breakage in 3-point bending tests. Ammar I B et al. [9] have investigated that PVC foam density can affect AE amplitude and counts distributions of different damage mechanisms under 4-point bending.

Therefore, as can be seen in Table 1, the existing results are always related to foam and honeycomb cored sandwiches. Characteristics of different AE parameters correlated to complicated damage modes of balsa cored sandwich are still unknown. Moreover, most researchers have used just one or two parameters to classify damages of sandwich structures. In order to achieve a more convincing description of the damage sequence and classification of more than four damage modes [6–8] of heterogeneous balsa sandwich structures, this work aims at the characterisation of damage mechanisms of a GFRP-balsa sandwich under static 4-point bending with the help of a new two-step clustering process of AE signals. The tested specimens have an original geometry [31,32], named triple dog-bone shape, which facilitates the observation of possible skin damages in the middle of the pure bending zone and core damages in the middle of the bending/shear zone under 4-point bending. This shape will benefit the classification of AE signals based on a better understanding of the real damage modes and locations. To correlate AE clusters to damage modes from different constituent materials [33] of GFRP-balsa sandwich, a two-step clustering process coupling the three most relevant AE parameters (amplitude, peak frequency and duration) has been proposed in this work. It contributes to better applying the popular K-means clustering method [28–30,34,35] to AE analysis of damage mechanisms of the complex GFRP-balsa sandwich.

In order to validate the damage characterisation results obtained by the proposed two-step AE clustering analysis approach, not only the

Table 1
Characteristics of AE parameters of composite sandwich structures.

References	Materials	Loading condition	Sensor type	AE parameters	Core damage	Skin/core debonding	Matrix cracking	Fiber breakage
Quispitupa A et al. [27]	CFRP-honeycomb	Tensile test	Two piezoelectric sensors	Amplitude (dB)	45–60	60–80	80–90	above 90
Fotouhi M et al. [13] and Pashmforoush F et al. [28]	GFRP-foam	DCB tests	Two resonance sensors (513.28 kHz)	Amplitude (dB) Dominant Frequency (kHz)	40–60 35–65	60–80 100–130	75–85 170–250	85–105 350–450
Tabrizi I E et al. [29]	GFRP-honeycomb	3-point bending	Two resonance sensors (550 kHz)	Duration (μs) Peak Frequency (kHz)	0–500 300–500	0–550 70–250	0–350 0–70	350–1000 0–120
Masmoudi S et al. [12]	E-glass fiber-PVC foam	3-point bending	Four WB sensors (100 kH-1 MHz)	Amplitude (dB)	41–60	72–93	41–78	above 92
Assarar et al. [30]	E-glass fiber-PVC foam	3-point bending	Two WB sensors (100 kH-1 MHz)	Amplitude (dB)	–	50–90	40–65	80–100
Ammar I B et al. [9]	E-glass fiber-PVC foam	4-point bending	Two WB sensors (100 kH-1 MHz)	Amplitude (dB)	30–70	80–90	60–80	above 90

post-mortem microscopic observations of fracture surfaces of GFRP skin and balsa core have been performed, but also some GFRP-balsa sandwich specimens [33] were further loaded up to a certain level below the fracture one (stopped tests). In particular, during the two-step clustering process, the determination of the optimum cluster number has been proven by combining different indices such as DB, Tou and Silhouette coefficients [36–39]. Finally, a clear and detailed description of correlations between the three AE parameters and damage mechanisms of GFRP-balsa sandwich has been concluded.

2. Experimental details

2.1. Materials and specimens

In this work, GFRP-balsa sandwich specimens with the special triple dog-bone shape [31,32] (see Fig. 1) were tested under 4-point bending and monitored by AE system. All sandwich specimens were fabricated using the vacuum resin infusion method, by infusing and curing the skin and core simultaneously. According to supplier standard of EPOLAM 2017 Resin, a big sandwich panel (1200 mm * 600 mm) was firstly cured in vacuum under room temperature for 7 hours, and then post-cured at 45 °C for 2 hours, 60 °C for 2 hours and 80 °C for 8 hours. Finally, the panel was cut into small triple dog-bone specimens by water jet technique. The interest of this original triple dog-bone shape is to observe more clearly the possible skin damages in pure bending zone 1, and core damages in bending and shear zone 2. Another advantage of using this special shape is to reduce the local stress concentrations under the loading supports and ensure the stability of the tests. All specimens have two identical symmetrical skins which are made of 3-layer GFRP weave balanced fabric/epoxy (Ref: Sicomin E glass fiber twill 3190 with 190 g/m^2, with 50% fiber volume fraction), and all layers are in the same direction to obtain the laminate of $[0^o]_3$. The core of GFRP-balsa sandwich is made from balsa wood (Ref: BALTEK SB.100, density: 148 kg/m^3), whose fibers are oriented in their thickness direction (Direction Z in Fig. 1. (b)). Material parameters of woven GFRP skin and balsa wood are the same as those illustrated in Refs. [32,33]. Dimensions of sandwich specimens are shown in Fig. 1. (a) and Table 2.

For the recycled balsa wood core, the original balsa wood panels are fabricated by bonding small blocks [33]. When the large balsa panel is cut into smaller specimens, different number of balsa/balsa block interfaces will be distributed randomly in the specimens, and these random interfaces may result in different shear stress distributions and AE responses under 4-point bending. The different positions of the balsa/balsa block interfaces in triple dog-bone GFRP-balsa sandwich specimens are illustrated in Fig. 2. Specimen 1 and specimen 2 were tested under 4-point bending up to its fracture, while the bending tests on specimen 5 and specimen 6 were stopped before its fracture at a predefined level. For specimen 1, there are two balsa/balsa block interfaces in zone 2. For specimen 2, there are three balsa/balsa block interfaces in zone 2. There is also one balsa/balsa block interface in the middle of zone 1 of specimen 2. As a comparison, the balsa/balsa block interface distributions of specimen 1 and specimen 5 are similar, while those of specimen 6 are similar to specimen 2. The influence of these balsa/balsa block interface positions on the received AE signals by sensors will be discussed in the following sections.

In addition, to identify AE signals coming from the balsa core material, the same 4-point bending tests were also conducted on pure balsa wood triple dog-bone specimens (see Fig. 3), monitored by the same AE system setup. The pure balsa wood specimens have the same dimensions as shown in Table 2.

Table 2
Sandwich specimen dimensions.

Constituents	Length (mm)	Max width (mm)	Min width (mm)	Thickness (mm)
GFRP (1 skin)	280	70	40	0.5
Balsa wood	280	70	40	9

2.2. Static 4-point bending test setup

Five GFRP-balsa sandwich specimens were tested under the same loading condition under room temperature, controlled by displacement rate imposed at 2 mm/min [32] using the MTS machine with a load cell of 100 kN. As seen in Fig. 4, the loading span (L) is 80 mm and the support span (S) is 240 mm. AE monitoring system is composed of two wideband sensors (100 kHz-1 MHz), two pre-amplifiers, some analog filters and a PCI-2 acquisition system (Mistras AEwin software). Two wideband sensors were chosen in order to allow the received signals not to be limited in certain resonance frequencies in the case of a multi-material structure. The sensors were glued on the skin surface symmetrically relative to the center of the specimen using a couplant (silicone grease), with a distance (D) of 180 mm, in order to receive all possible AE hits within a large frequency range generated in zone 1 and 2 during 4-point bending tests. After many preliminary tests, the threshold which determines the system sensitivity to the environmental noise, was set by 28 dB. The most important AE acquisition parameters [33] are shown in Table 3. Peak Definition Time (PDT), Hit Definition Time (HDT) and Hit Lockout Time (HLT) are the critical ones which make sure that complicated AE waveforms are cut into the right number of hits. PDT ensures correct identification of risetime of peak amplitude. HDT ensures that each AE signal from the structure is reported as one and only one hit. With proper setting of HLT, useless measurements during the signal decay are avoided and data acquisition speed can be increased. For composite structures, it is suggested in Aewin user manual that PDT is within 20–50 μs, HDT within 100–200 μs, and HLT be 300 μs. After some testing, finally, for GFRP-balsa sandwich under 4-point bending, PDT is 30 μs, HDT is 100 μs, and HLT is 300 μs.

3. The new two-step clustering process in AE analysis

After a comparative study of different clustering algorithms at our disposal, statistical treatment of AE signals by K-means algorithm [28–30,34] built in NOESIS software has been performed to classify AE hits into different cluster groups, as so to correlate AE clusters to different damage mechanisms of GFRP-balsa sandwich. Herein, the selection of optimum AE parameters and the optimisation of the suitable cluster number are the key factors to generate the most robust damage classification results [35,36]. Eleven most common AE parameters are chosen here to keep the most correlated AE features and improve the efficiency of the algorithm: energy, amplitude, duration, rise time, counts, counts to peak, average frequency, frequency centroid, peak

(a) Geometry (mm) of triple dog-bone sandwich (b) Loading condition and specimen shape

Fig. 1. The geometry of GFRP-balsa sandwich specimens.

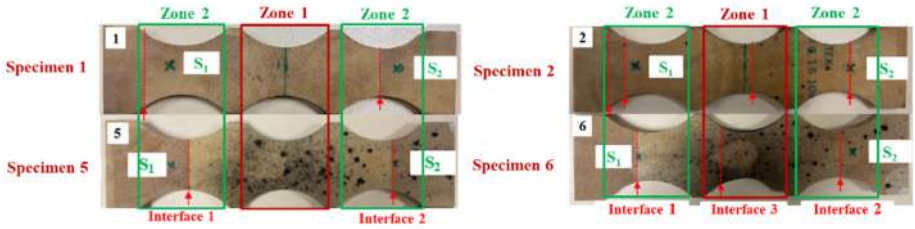

Fig. 2. Positions of sensors and balsa/balsa block interfaces in GFRP-balsa sandwiches in non-stopped (specimens 1 and 2) and stopped tests (specimens 5 and 6).

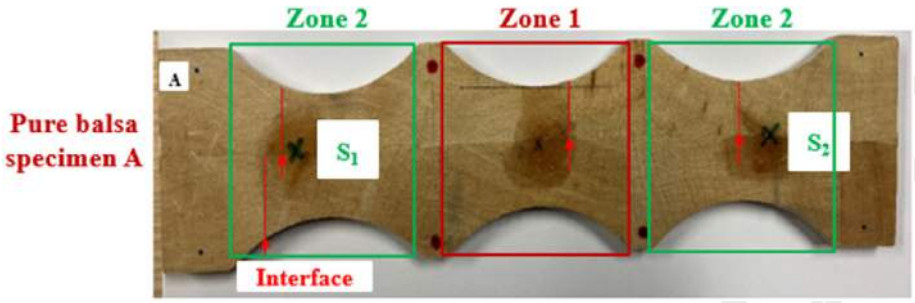

Fig. 3. Positions of sensors and balsa/balsa block interfaces in pure balsa specimen A.

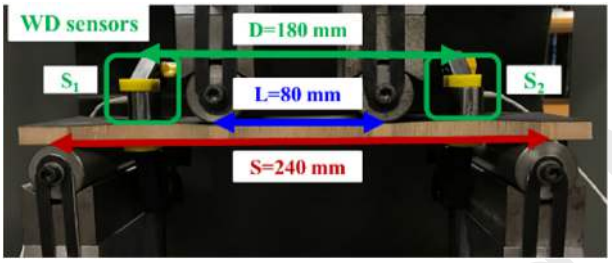

Fig. 4. 4-point bending test monitored by AE wideband sensors.

frequency, initiation frequency and reverberation frequency, which have been proven by the previous work [10,34] of our laboratory on composites and woods. A normalisation of the data between 0 and 1 was carried out to limit the weight of certain parameters such as the high energy values. To determine the optimum cluster number k, Davies & Bouldin (DB), Tou and Silhouette coefficients [37–39] have been chosen in this work.

DB is the mean value of the max ratio of the average intra-cluster distance to the average inter-cluster distance, as Eq. (1) shows. The cluster number k is optimum when DB is minimum.

$$DB \quad \frac{1}{k}\sum_{i\ 1}^{k} \max\left(\frac{d_i + d_j}{d_{ij}}\right) \tag{1}$$

Where d_i and d_j are the average intra-distance within the class i and j, respectively; d_{ij} is the inter-cluster distance between the class i and j; i, j, k 1, 2, …, n; i/j.

Tou is defined as the ratio of the minimum inter-distance between any pair of clusters to the maximum average intra-cluster distances, as Eq. (2) shows. It does not consider the average ratio, so it is often used as the complement validation of DB. The higher Tou is, the higher the discrimination efficiency will be.

$$Tou \quad \frac{\min(d_{ij})}{\max(d_i)} \tag{2}$$

Where d_{ij} is the inter-distance between the class i and j; d_i is the average intra-distance within the class i; i, j, k 1, 2, …, n.

Silhouette coefficient is the difference between the average inter-cluster distance and the mean intra-cluster distance, normalized by the maximum value, as Eq. (3) shows. It is a measure of how similar an object is to its own cluster (cohesion) compared to other clusters (separation). It produces a score between 1 and -1, where 1 is highly dense clusters and 1 is completely incorrect clustering. Through PYTHON algorithm, the mean Silhouette score can be computed by averaging the silhouette coefficient of each cluster.

$$S\ ilhouette \quad \frac{b_i \quad a_i}{\max(a_i, b_i)} \tag{3}$$

Where, a_i is the average intra-distance between each point within a cluster i. b_i is the average inter-distance between all clusters.

It should be kept in mind that all these indices could be affected by the amount of the database and the real damage types which might be unknown before AE analysis. So, the real damage mechanisms observed by microscope and the statistical indices of K-means method should be associated to make a good decision about the choice of optimum cluster number.

In this work, based on Table 1 concluded from literatures, more than four damage modes in GFRP-balsa composite sandwich structures could be generated under 4-point bending. To classify more than four damage modes by AE monitoring, we have proposed a new two-step clustering process through K-means method, as described by the flow chart in Fig. 5. The three most relevant AE parameters including amplitude, peak frequency and duration have been analyzed detailedly to find the correlations between damage mechanisms and AE signals. On the basis of

Table 3
AE acquisition parameters for GFRP-balsa sandwiches under 4-point bending.

Threshold (dB)	Pre-amplifier (dB)	Analog Filter (MHz)	PDT (μs)	HDT (μs)	HLT (μs)	Sample Rate (MSPS)	Pre-Trigger (μs)	Hit Length
28	40	0.02–3	30	100	300	5	50	4k

the anisotropic properties of both the balsa core and laminate skins, this two-step clustering process approach is suggested in AE analysis when there are two obviously different kinds of materials in a sandwich structure. The two-step clustering process is as following:

Step 1 Based on DB/Tou/Silhouette indices and microscopic observations of damage surfaces, a first clustering process should be performed on the received AE signals to filter the signals corresponding to microscopic balsa core damages (Cluster 0). The rest of signals should come from skin damages and skin/core debonding (Cluster I).

Step 2 Based on DB/Tou/Silhouette indices and microscopic observations of damage surfaces, a second clustering process should be further performed on Cluster I, to classify skin damages and skin/core debonding. In this step, the cumulative counts of Cluster I should be calculated to identify initiation of different damage modes of GFRP skin, based on the three transitions points of the cumulative curve [32,40,41]. And then, amplitude, peak frequency and duration should be combined to identify skin/core debonding, mainly based on the higher peak frequency range.

Finally, the correlations between the AE parameters and more than four damage modes of balsa composite sandwich structures can be concluded. The validation of this new two-step clustering process in AE analysis will be discussed in detail below.

4. Static 4-point bending behavior of GFRP-balsa sandwich

4.1. Bending stiffness and strength

Force/Displacement curves of four sandwich specimens under 4-point bending loading are plotted in Fig. 6. The average bending stiffness and fracture load are 102 N/mm (±4 N/mm) and 1125 N (±92 N), respectively. In the following sections, bending responses of specimens 1 and 2 will be compared because they represent well those of the other two specimens, and they show the very obvious difference from AE signals received by the two wideband sensors.

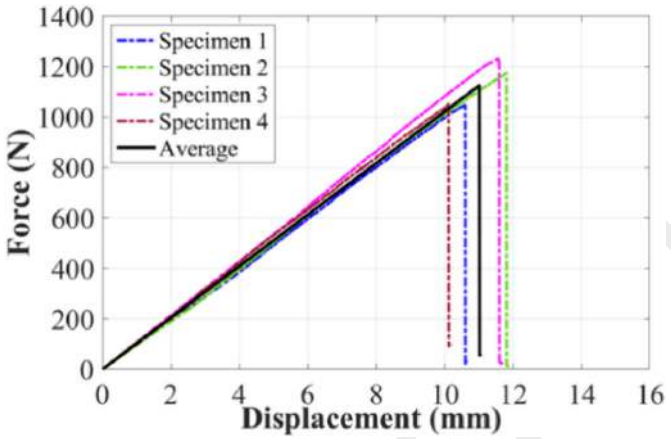

Fig. 6. Force/Displacement curves of GFRP-balsa sandwiches under static 4-point bending.

4.2. Fracture surface observations by microscope

At the end of 4-point bending tests, it can be visually observed that compressive damages of the upper GFRP skin in pure bending zone 1 are the predominant damage modes (see Fig. 7) in all sandwich specimens. Before analyzing AE signals, microscope VHX-7000 (100 X) was used to observe the damage details of the smaller zone S in center of the upper GFRP skin in pure bending zone 1 at the end of 4-point bending tests, as shown in Fig. 8. The white areas observed on the GFRP skin indicate that

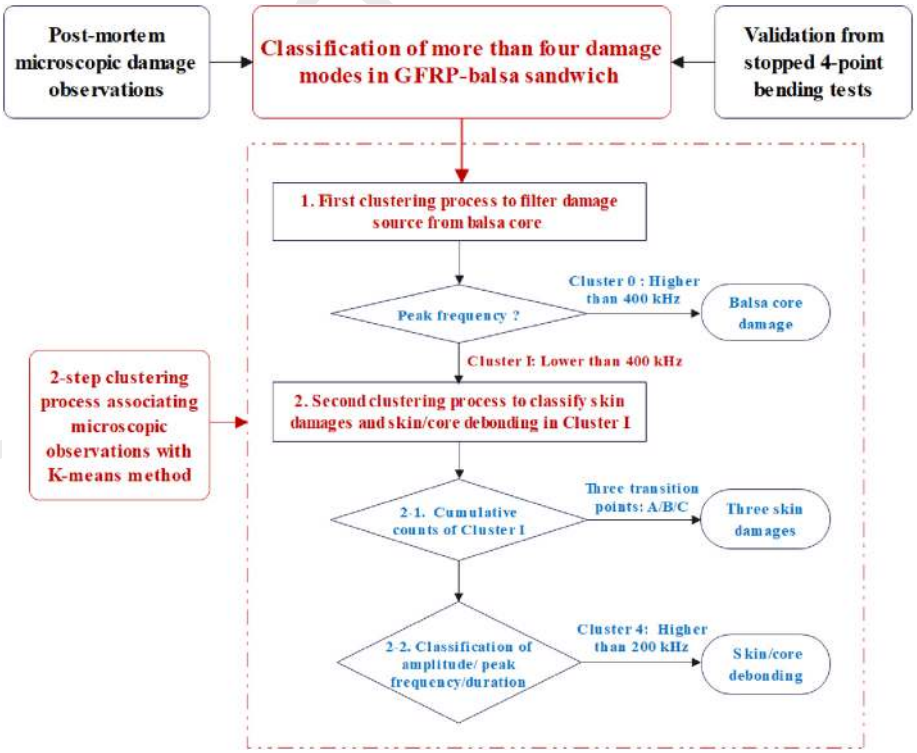

Fig. 5. Flow chart of the proposed two-step clustering process in AE analysis of balsa cored sandwich.

(a) Specimen 1 (b) Specimen 2

Fig. 7. Fracture surfaces of GFRP-balsa sandwiches after 4-point bending tests.

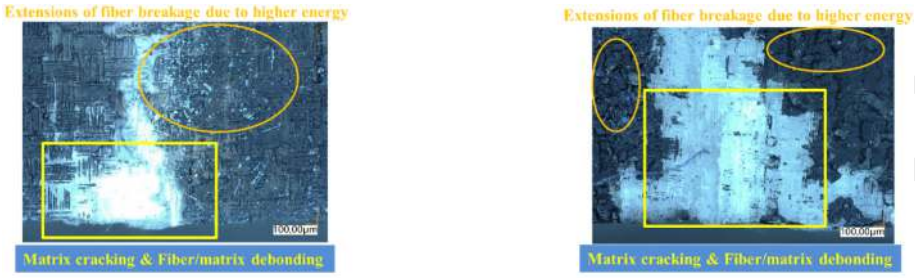

(a) Specimen 1 (b) Specimen 2

Fig. 8. Upper skin damage images of GFRP-balsa sandwiches after 4-point bending tests (zone S).

glass fiber ends are obviously visible [13] and some resins have disappeared. These white areas will be compared to images observed in the later stopped tests to show more clearly the initiation of matrix cracking and fiber/matrix debonding. The small extensions of fiber breakage pointed out by the cycles have been caused by dynamic effect of higher energy released within very short time at the final fracture time [32]. Fig. 9 also exposes the side view observations of GFRP skin and balsa core damages in center zone C. It is interesting to note that specimen 2 has a skin/core debonding crack of 6 mm which is 20% longer than that in specimen 1 (5 mm), which will be an important physical mechanism to help distinguish AE signals correlated to skin/core debonding. In addition, no visible core damage can be observed by the microscope in zone 2 which is loaded by bending moment and shear force.

In summary, under 4-point bending, microscope observations indicate that the predominant damages of GFRP-balsa sandwich could be GFRP skin damages containing matrix cracking, fiber/matrix debonding, delamination and fiber breakage [10,12,13,30,32], accompanied by a few skin/core debonding cracks [1,2] which have no significant effect on the global bending stiffness and fracture load of the sandwich. All these observations can help verify the next clustering results of AE signals.

5. Damage mechanism characterisation by two-step clustering process in AE analysis

5.1. First step of clustering process: filtering microscopic balsa core damages (Cluster 0)

5.1.1. Identification of balsa core damages

Based on the proposed AE analysis approach in Fig. 5, the traditional K-means clustering process was firstly applied to the original test data. Amplitude and peak frequency were firstly chosen to correlate AE features with different damage modes. Fig. 10 shows the calculated DB/Tou/Silhouette indices, to determine optimum number of clusters. When cluster number is 2, DB is lowest, Tou is highest, and Silhouette coefficient is closest to 1, so cluster number 2 is finally chosen for all specimens. Combining damage mechanisms observed by microscope and DB/Tou/Silhouette indices, the reason why cluster number 2 is optimum is that the two distinctly different constituent materials may result in two different kinds of damage sources in sandwich structure. It is also interesting to find that the lowest DB of cluster number 2 is more obvious for specimen 2 who contains more balsa/balsa block interface, so specimen 2 has released more balsa core damage sources. It indicates that when AE hits from balsa core become more important, the DB index will become more effective due to a larger amount of data in the group of microscopic balsa damage. That's just the interest to compare specimen

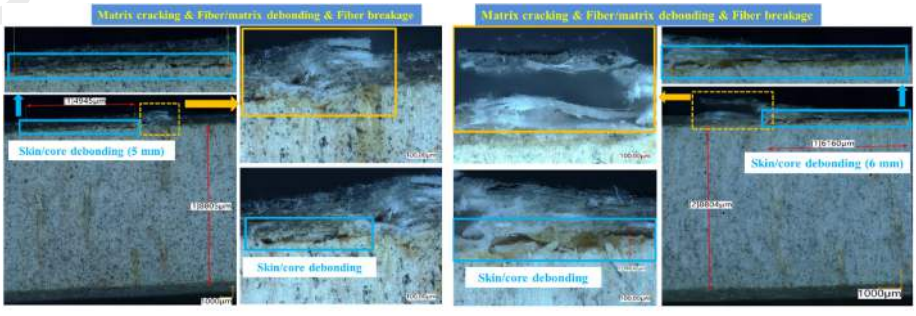

(a) Specimen 1 (b) Specimen 2

Fig. 9. Skin and core damage images of GFRP-balsa sandwiches after 4-point bending tests (zone C).

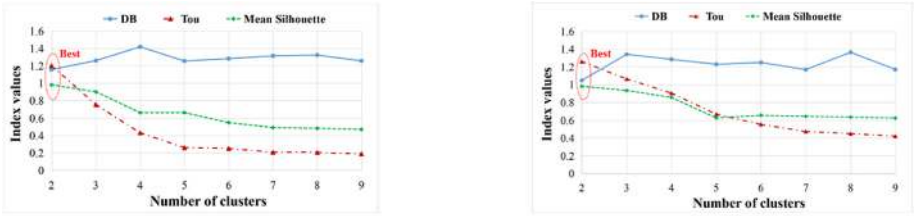

(a) Specimen 1 (b) Specimen 2

Fig. 10. Determination of the optimum number of clusters in the first clustering process.

1 and specimen 2 to find the difference of correlation between damage mechanisms and AE signal accumulation. In Fig. 11, the two clustering groups based on amplitude and peak frequency distributions from sensor S_1 of the two specimens 1 and 2 are compared to Force/time curves. Sensor S_1 has been chosen because S_1 has received more AE hits compared to S_2.

Firstly, it can be seen that the higher amplitude signals accumulate intensely just at the final fracture time of specimen 1 and before the fracture load of specimen 2. It is interesting to find that most signals within Cluster 0 of the two specimens are lower than 60 dB and within a

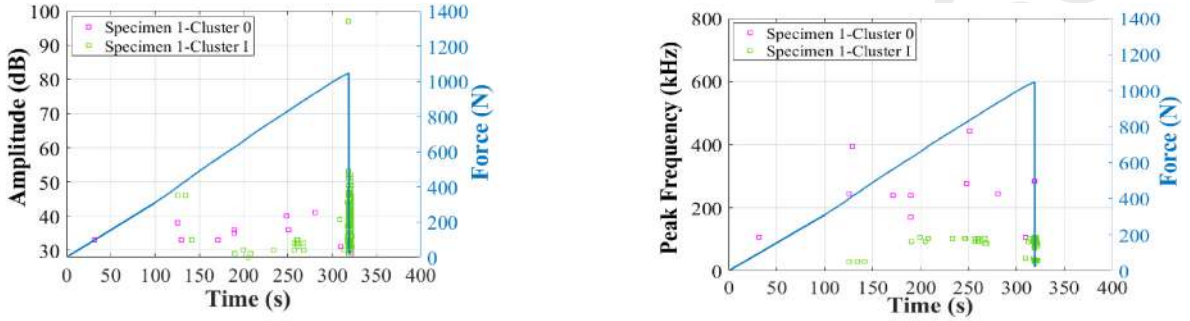

(I) Amplitude vs. Time (II) Peak Frequency vs. Time

(a) AE signals from specimen 1

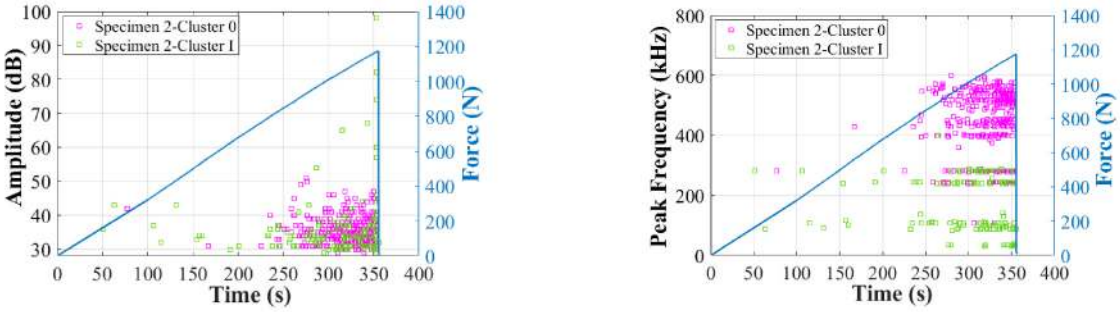

(I) Amplitude vs. Time (II) Peak Frequency vs. Time

(b) AE signals from specimen 2

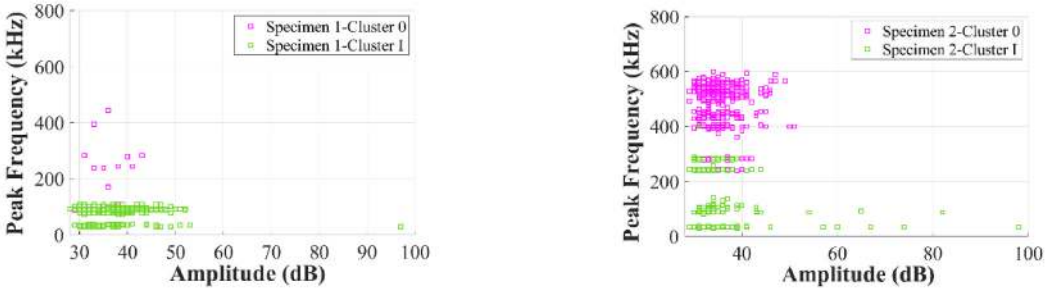

(I) Specimen 1 (II) Specimen 2

(c) Peak Frequency vs. Amplitude

Fig. 11. The two clusters after first clustering process of GFRP-balsa sandwiches.

higher frequency range of 200–600 kHz. While Cluster I contain the highest amplitude above 90 dB and the peak frequency range is lower than 400 kHz. Referred to Table 1, Cluster I may include the predominant GFRP skin damages and skin/core debonding, and the highest amplitude signal should come from fiber breakage. Based on the possible damage mechanisms of GFRP-balsa sandwich under 4-point bending observed by the microscope in Figs. 8 and 9, Cluster I should contain matrix cracking, fiber/matrix debonding, delamination, fiber breakage and skin/core debonding.

Because skin damages also include low amplitude damage modes such as matrix cracking, it's difficult to just dissociate Cluster 0 from Cluster I only by amplitude, but it becomes much easier by peak frequency. When comparing AE signals between specimen 1 and specimen 2, the typical difference is that Cluster 0 of specimen 2 takes up a more proportion within higher peak frequency range.

In order to find explanations for this observation, it should recall that the main material difference between specimen 1 and 2 is the different positions of balsa/balsa block interfaces, as illustrated in Fig. 2. For example, for specimen 1, there are two interfaces between balsa blocks in zone 2, one is very near to sensor S_2, and the other is near to sensor S_1. For specimen 2, there are three balsa/balsa interfaces in zone 2, one is exactly below the sensor S_2, and the other two are near to sensor S_1. One the one hand, considering the core shear stress distributions in zone 2 of sandwich structures under 4-point bending loading, different balsa/balsa block interfaces could induce different levels of microscopic interfacial damages between balsa blocks. On the other hand, from the view of AE, different distances between the sensors and balsa/balsa block interfaces could have sensitive effects on the number of hits within Cluster 0 received by different sensors. When the sensor is put nearer to the balsa/balsa block interfaces and there are more interfaces in core shear zone 2, more AE signals within Cluster 0 could be received. Finally, signals of sensor S_1 were chosen to better discriminate core damages of specimen 1 and specimen 2. Then it can be understood that S_1 of specimen 1 receives fewer signals coming from cluster 0 than S_1 of specimen 2, verifying that Cluster 0 could be related to balsa core damages.

5.1.2. Validation from pure balsa specimens under the same 4-point bending

The above analysis signifies that Cluster 0 may be dominated by damages in balsa core, but these damages cannot be observed by microscope. To validate the real mechanisms of Cluster 0 which appear relatively early at the beginning in Fig. 11, 4-point bending tests on two pure balsa wood specimens (see Fig. 2) under the same loading condition have been conducted, monitored by the same AE system setup. The responses of these two specimens are very close. There is no visible balsa wood damage at the end of the bending test even though the final displacement is near to 12 mm. The stiffness of the tested pure balsa specimens remains almost unchanged from the intact one. However, interestingly, some AE signals have been received during the tests. The damage associated with these signals should be at microscopic scale, which it doesn't influence the global stiffness of the pure balsa specimen.

Afterwards, only AE results from pure balsa specimen A will be discussed. Force/time curves and AE parameter distributions from sensor S_1 of the pure balsa specimen A are shown in Fig. 12. It is interesting to find that pure balsa wood specimens can release AE signals lower than 50 dB and within a higher frequency range of 200–600 kHz even though no obvious cracks can be visible, as shown in Fig. 12. (a)–(c).

Another interesting result is that these signals have a duration less than 200 μs, as seen in Fig. 12. (d). So, Fig. 13 further shows the correlations between peak frequency/duration and amplitude of Cluster 0 of sandwich specimen 2 which should receive more signals from balsa core. It can be seen that there are more signals less than 200 μs within 200–600 kHz and 30–50 dB in Cluster 0 of sandwich specimen 2, compared to pure balsa specimen. Fig. 13. (b) also highlights the importance of duration to help further classify different damage modes of balsa sandwich structures.

In conclusion, although the stress distributions of pure balsa specimen and balsa core of the sandwich are not the same under the same 4-point bending loading condition, AE parameter distributions of pure balsa can help us to verify that peak frequency of AE hits coming from microscopic damages of balsa wood core is mainly within 200–600 kHz, with amplitude lower than 50 dB and duration less than 200 μs. However, the detailed damage mechanisms of balsa wood core need further investigations, which may include microscopic cracks, balsa/balsa block

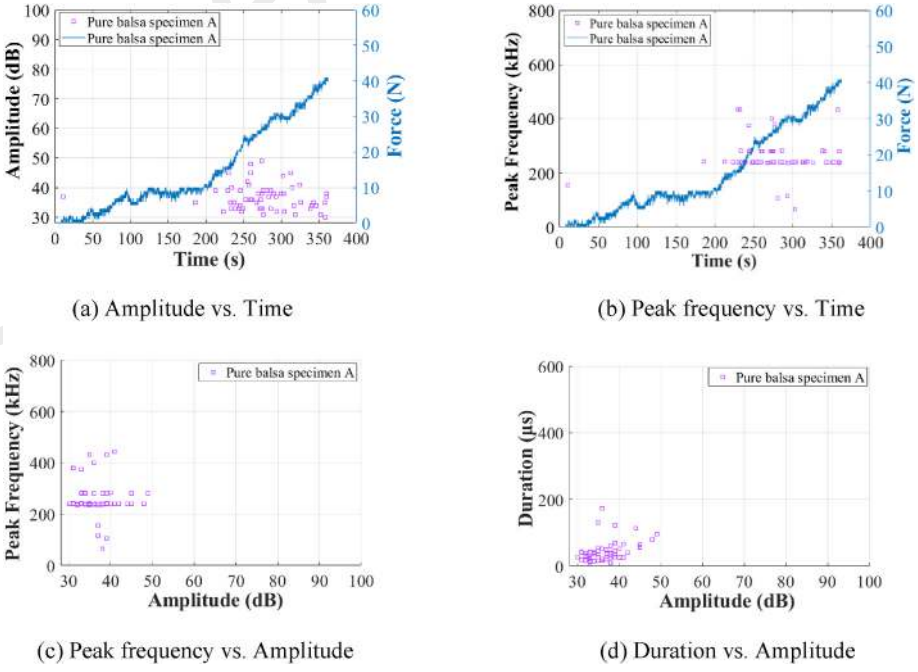

Fig. 12. AE parameter distributions from sensor S_1 of pure balsa specimen An under 4-point bending.

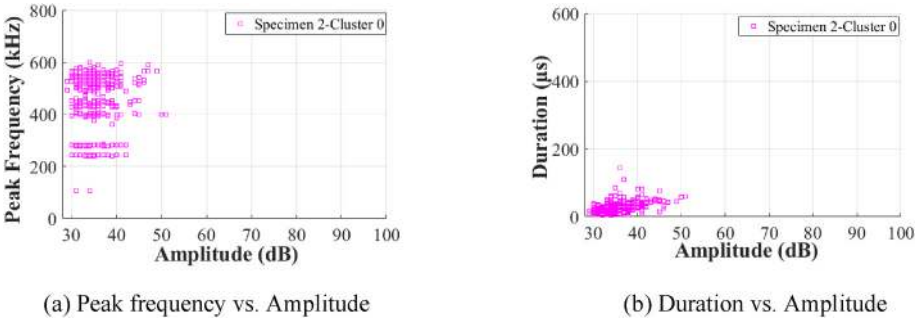

Fig. 13. Duration/Peak frequency vs. Amplitude of Cluster 0 of GFRP-balsa sandwich specimen 2.

interface debonding and propagation of balsa cracks [33].

5.2. Second step of clustering process on Cluster I: identification of skin damage modes and skin/core interface damage

5.2.1. Identification of skin damage initiation based on cumulative counts

After filtering the AE signals corresponding to balsa core damages (Cluster 0), the signals in Cluster I should come from the skin and skin/core interface damages. For composite laminate damages, cumulative counts have been proven to be effective for the identification of the crack front, crack opening and crack propagation path [11,20], while cumulative acoustic energy can be used to mainly identify the crack opening and propagation in the fiber reinforced composites. Oskouei et al. [40] have observed AE energy only at the onset of delamination of laminates and no signal has been recorded before that in mode I fracture tests. But it is still not clear whether these cumulative parameters can be useful for the damage initiation indication of laminate skin damages in a complex heterogeneous sandwich. In this work, cumulative counts accumulation of Cluster I of GFRP-balsa sandwich specimens are firstly investigated to identify the damage initiation of all possible skin damages, as seen in Fig. 14. It shows obviously that cumulative counts could be very useful for the detection of three transition Points A, B and C here.

In Fig. 14, according to the damage mechanisms of composite laminates, Point A should be the damage initiation of microscopic matrix cracking [41], Point B should be the initiation of macroscopic crack, for example, fiber/matrix debonding, and Point C should be the start of the propagation of delamination and final fiber breakage [32,40,41]. Based on these interesting findings, next, the correlations between three AE parameters and Force/Time curves will be discussed in detail to further identify skin/core debonding and classify different damage mechanisms of GFRP skin.

5.2.2. Distinguish of skin/core debonding from skin damages based on AE multi-parameters

5.2.2.1. AE amplitude distributions. In order to further distinguish skin/core debonding from complex skin damages, the second clustering process was performed on Cluster I. For the two specimens, Fig. 15 exposes that the optimum cluster number is four when DB is lowest, Tou is relatively higher and Silhouette is closer to 1. According to discussions in Refs. [37–39], it is sometimes difficult to determine the optimum number of clusters particularly in glass fiber composites, because the different indices DB, Tou and Silhouette do not always meet the theoretical criteria at the same time. Indeed, the lack of large amounts of data could result in unclear number of clusters. But the majority case is that DB is the most effective index for most GFRP composites compared to

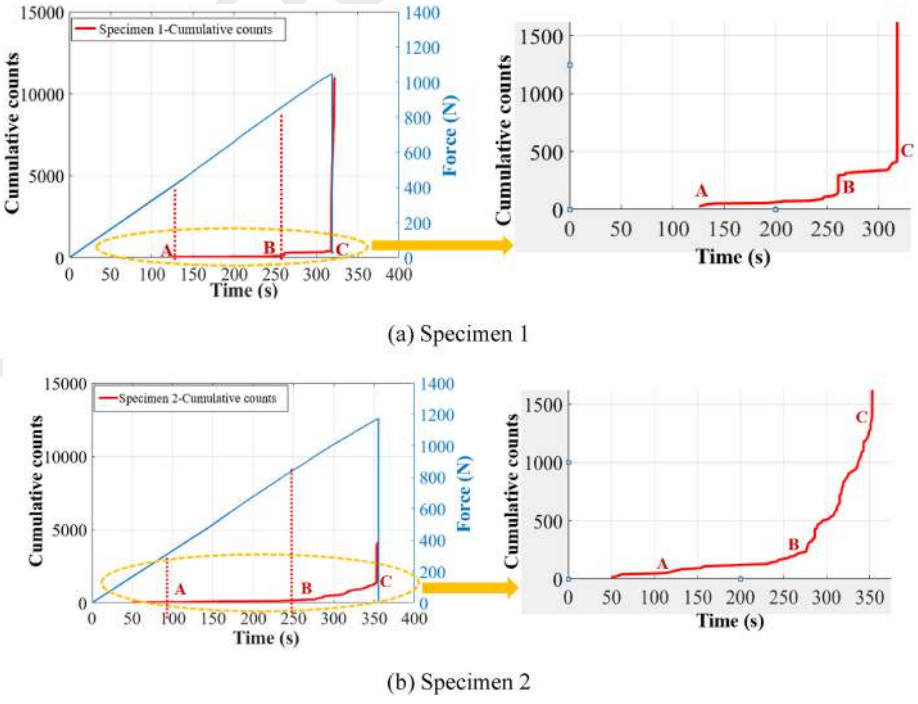

Fig. 14. Cumulative counts of Cluster I vs. time of GFRP-balsa sandwiches.

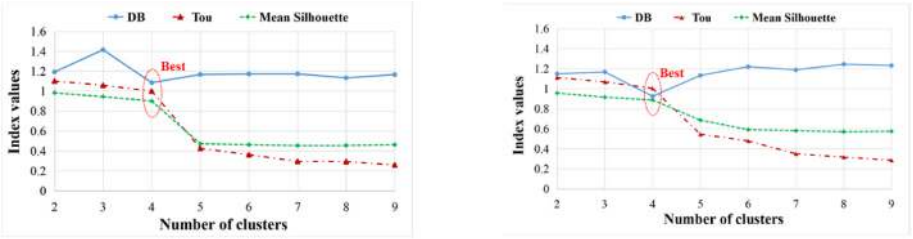

Fig. 15. Determination of the optimum number of clusters in the second clustering process.

other indices in related literatures. One reason could be that Tou or Silhouette considering the max intra-distance may become less accurate when database is not so rich, based on Eq. (2) and Eq. (3) in section 3. Further work on more suitable criteria will have to be verified in the future. Similar to the first clustering process, because skin/core debonding crack of specimen 2 is longer as observed by microscope, more AE signals have been released by specimen 2 in the cluster group related to skin/core debonding. As a result, the database is richer, so DB index is more effective for specimen 2. The four clusters decomposed from Cluster I will be named as Cluster 1, 2, 3 and 4 in the following discussions.

Firstly, AE amplitude distributions of Cluster 1–4 are compared to Force/time curves in Fig. 16. It shows that signals accumulate intensely just at the final fracture time for specimen 1 and before the final fracture for specimen 2. As identified by cumulative counts (see Fig. 14), Points A, B and C are also marked in Fig. 16. Firstly, Cluster 1 and Cluster 4 are predominant during the stage AC, lower than 50 dB. Considering the damage initiation time of laminates [30], matrix cracking and fiber/-matrix debonding should be included in Cluster 1. Combined with microscope observations, Cluster 4 could be skin/core debonding which is more severe in specimen 2, but it needs further validation from other AE parameters. In addition, although two signals of Cluster 2 also appear at the beginning, all the other signals of Cluster 2 mainly accumulate near Point C in stage BC. Cluster 3 mainly appears just at Point C. The highest amplitude of Cluster 3 is above 90 dB, so it should correspond to the final fiber breakage [12,30] which only appears at Point C. Cluster 2, which appears just before fiber breakage with the intermediate amplitude range of 40–70 dB, should be GFRP skin delamination [30].

In addition, it can be seen that specimen 2 has shown a little more obvious non-linear behavior at the end of the tests, and the transition point between linear and non-linear behavior is just Point B. It indicates that Point B and C should be the important indicators of irreversible macroscopic damages including fiber/matrix debonding (in Cluster 1), delamination (Cluster 2) and fiber breakage (Cluster 3).

5.2.2.2. AE duration distributions. Fig. 17 compares the duration distributions of sandwich specimen 1 and specimen 2. Similar to the analysis of amplitude, for both specimens, before Point B, most of the signals show very short duration less than 500 μs, dominated by Cluster 1 and Cluster 4. After Point B, especially at Point C, more signals higher than 500 μs in Cluster 1 accumulate, and these signals should come from fiber/matrix debonding [29]. Duration of Cluster 4 is always very short, mainly less than 500 μs, especially in specimen 2. Thus, duration is a very important parameter to identify skin/core debonding (Cluster 4) from fiber/matrix debonding (Cluster 1). At the fracture moment C, durations of cluster 2 and 3 are much higher. Cluster 2 is less than 2000 μs, while Cluster 3 is mainly higher than 2000 μs. So, duration can be also an important indicator to distinguish delamination and fiber breakage which appear almost simultaneously. As a validation, in Ref. [29], duration of GFRP skin/honeycomb core debonding under 3-point bending is 0–550 μs, a little higher than 0–350 μs of matrix cracking, and lower than 350–1000 μs of fiber breakage, similar to duration range difference in this work.

5.2.2.3. AE frequency distributions. Peak frequency is the point where the power spectrum is greatest. Fig. 18 further compares peak frequency distributions of sandwich specimen 1 and specimen 2. Fig. 19 also shows more clearly the relationship between peak frequency and amplitude of sandwich specimen 1 and specimen 2. For specimen 1, all the signals have the frequency range lower than 200 kHz. For specimen 2, Cluster 1, Clusters 2 and 3 are mainly lower than 200 kHz, while Cluster 4 has more signals higher than 200 kHz, increasing greatly after point B. Combined with microscope observations, the main damage difference of these two specimens is the more obvious skin/core debonding crack in specimen 2. It indicates that Cluster 4 corresponds to skin/core debonding, which has a frequency range between the lower range of skin damages and higher range of core damages. It should be related to the different material properties of the two constituents. As a validation, it has been also found in Ref. [29] that skin/core debonding of GFRP-honeycomb sandwich is within 70–250 kHz under monitoring of wideband sensors in 3-point bending tests.

5.3. Summary

Finally, based on the above analysis from cumulative counts, clustering results coupling amplitude, duration and peak frequency distributions, validated by microscope observations, some useful conclusions can be made in Table 4. However, it shall be noticed that these

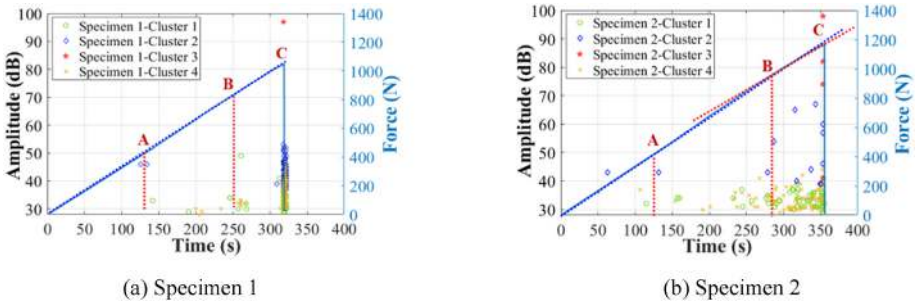

Fig. 16. AE amplitude distributions of GFRP-balsa sandwiches under 4-point bending.

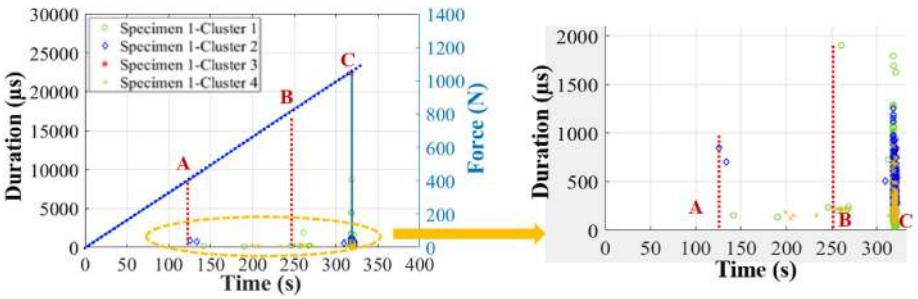

(a) Specimen 1

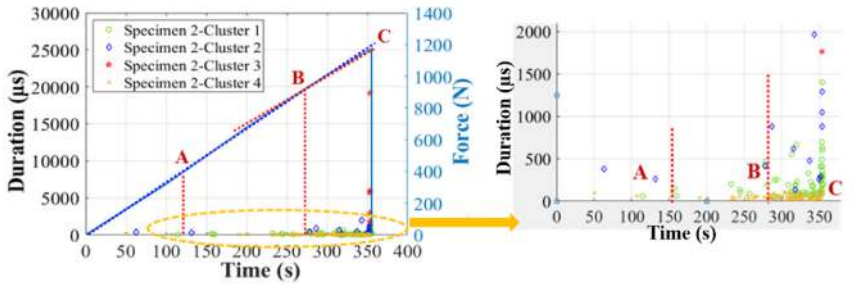

(b) Specimen 2

Fig. 17. AE duration distributions of GFRP-balsa sandwiches under 4-point bending.

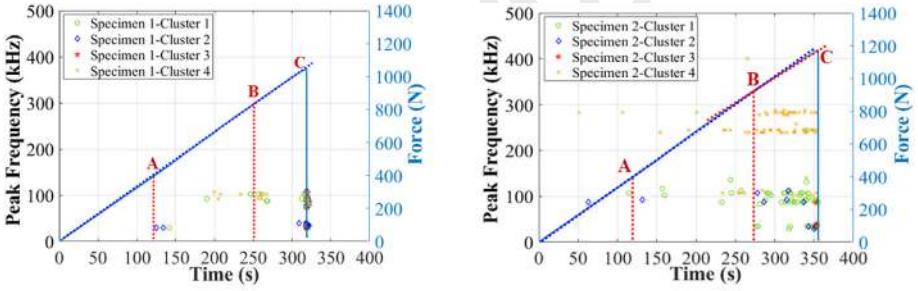

(a) Specimen 1 (b) Specimen 2

Fig. 18. AE frequency distributions of GFRP-balsa sandwiches under 4-point bending.

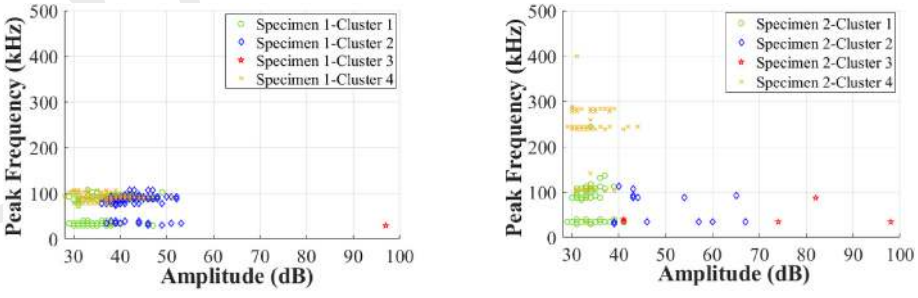

(a) Specimen 1 (b) Specimen 2

Fig. 19. Peak frequency vs. Amplitude of GFRP-balsa sandwiches under 4-point bending.

characteristics can be affected by the sensor types, loading condition and laminate stacking sequence and so on.

Table 5 further compares the dominance of Clusters 1–4 with Cluster 0 based on AE hits number. It is obvious that Cluster 0 of specimen 2 receives more signals due to microscopic balsa core damages. Among Cluster 1–4, the fraction of Cluster 1 of specimen 1 is higher than Cluster 2/3/4, while Cluster 4 of specimen 2 takes up larger proportion than Cluster 1/2/3. So, it matches well with microscope observations, verifying that specimen 2 has longer skin/core debonding crack.

Table 4
AE characteristics of GFRP-balsa sandwich under 4-point bending.

AE parameters	Cluster 0	Cluster 1	Cluster 2	Cluster 3	Cluster 4
	Microscopic balsa core cracks & Interfacial debonding	Matrix cracking & Fiber/matrix debonding	Skin delamination	Fiber breakage	Skin/core debonding
Amplitude (dB)	<50	<50	40–70	>70	<50
Duration (μs)	<200	<5000	<2000	2000–25000	<500
Peak Frequency (kHz)	200–600	20–200	20–200	20–200	80–400

Table 5
Dominance of different damage mechanisms of GFRP-balsa sandwiches under 4-point bending.

Specimen	Total	Cluster 0	Cluster 1	Cluster 2	Cluster 3	Cluster 4
		Microscopic balsa core cracks & Interfacial debonding	Matrix cracking & Fiber/matrix debonding	Skin delamination	Fiber breakage	Skin/core debonding
1	%:100	4.1	42.9	20.8	0.2	32.0
	Hits:515	21	221	107	1	165
2	%:100	71.2	11.5	2.3	0.9	14.1
	Hits:548	390	63	13	5	77

6. Validation of the proposed two-step clustering process in AE analysis by stopped 4-point bending tests

6.1. Bending responses of specimens 5 and 6 in stopped 4-point bending tests

To further validate the damage classification results in Table 4, in particular damage modes such as matrix cracking and fiber/matrix debonding before final fracture, sandwich specimens 5 and 6 (see Fig. 2) have been tested up to a certain load level, that is, the tests were stopped before the final failure. Fig. 20 shows Force/Time curves of specimen 5 stopped at 220 s in stage AB and specimen 6 at 275 s in stage BC, respectively. To better compare the different curves, Points B_1 and C_1 are marked specifically on specimen 1, while points B_2 and C_2 are on specimen 2.

As illustrated in Fig. 2, the balsa/balsa block interface distributions of specimen 1 and specimen 5 are similar, while those of specimen 6 are similar to specimen 2. For specimen 5, signals received by sensor S_1 are further classified because the distance between S_1 and its nearest balsa/balsa block interface is more similar to S_1 of specimen 1. For specimen 6, signals received by sensor S_2 are further classified because the distance between S_2 and its nearest balsa/balsa block interface is more similar to S_1 of specimen 2. Sensor S_2 of specimen 5 and sensor S_1 of specimen 6 are not chosen because they are put exactly on one of the balsa/balsa block interfaces, and they will receive more signals from balsa core damages within higher frequency range, but the main objective of the stopped test is to investigate the skin damages.

6.2. Damage mechanisms observed on specimens 5 and 6 by microscope

In order to better observe matrix cracking and fiber/matrix cracking, microscope VHX-7000 (100 X) images of the upper skin surfaces in zone 1 of specimens 5 and 6 were observed before starting the 4-point bending tests. As shown in Fig. 21, no visible damage can be found. Microscopic images of the damaged surfaces at the end of the stopped tests are also shown in Fig. 22-Fig. 23. For specimen 5, after the tests, matrix cracking in upper composite skins can be observed (see Fig. 22. (a)) and the onset of skin/core debonding can be seen but not obvious (Fig. 22. (b)). On the upper skin surface of specimen 6, apart from matrix cracking, fiber pull out can be seen, which demonstrates that more fiber/matrix debonding has appeared in stage BC (Fig. 23. (a)). Longer fiber/matrix debonding crack can be also seen in Fig. 23. (b), and it will induce the later delamination in the composite skin. Due to reduction of the strengths of the fiber/matrix interfaces and the infused resin at skin/core

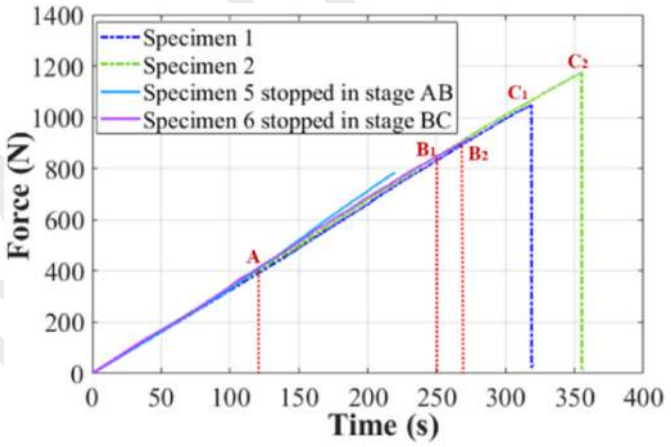

Fig. 20. Comparison of Force/Time curves of sandwich specimens in stopped and non-stopped tests.

interface, the small existence of onset of adhesive resin film debonding from the skin (skin/core debonding) can be also observed. For specimens 5 and 6, no fiber breakage can be seen. When comparing microscope images of skins in stopped tests with images in Fig. 8 in non-stopped tests, it is clear that white area which shows the disappearance of resins becomes larger after point B until the final rupture of the fiber. It means that matrix cracking and fiber/matrix cracking propagates faster after point B.

6.3. Identification of damage mechanisms based on the two-step clustering process

6.3.1. First clustering process: filtering balsa core damages

Based on the damage characterisation approach proposed in non-stopped 4-point bending tests, for specimens 5 and 6 in stopped tests, the signals coming from the balsa core are firstly identified by the first clustering process by K-means method using two cluster number. Fig. 24 and Fig. 25 show AE parameters of Cluster 0 of specimen 5 and specimen 6, respectively. It can be concluded that only few signals in Cluster 0 appear after 150 s, with amplitude lower than 50 dB, duration less than 200 μs, and peak frequency within 200–600 kHz. It matches well with the previous conclusions.

(a) Upper skin in zone 1 of specimen 5 (b) Upper skin in zone 1 of specimen 6

Fig. 21. Skin surface images of specimens 5 and 6 before 4-point bending tests.

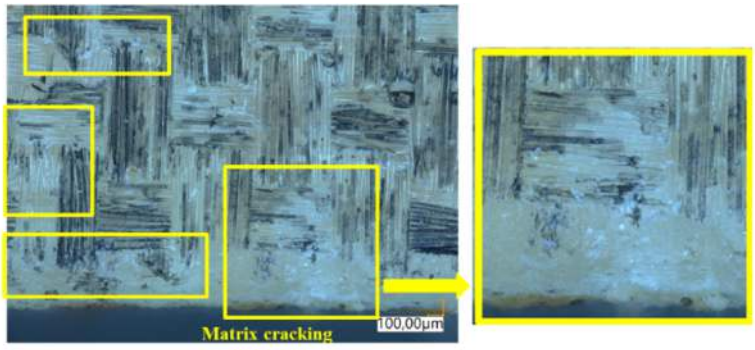

(a) Upper skin damages of specimen 5

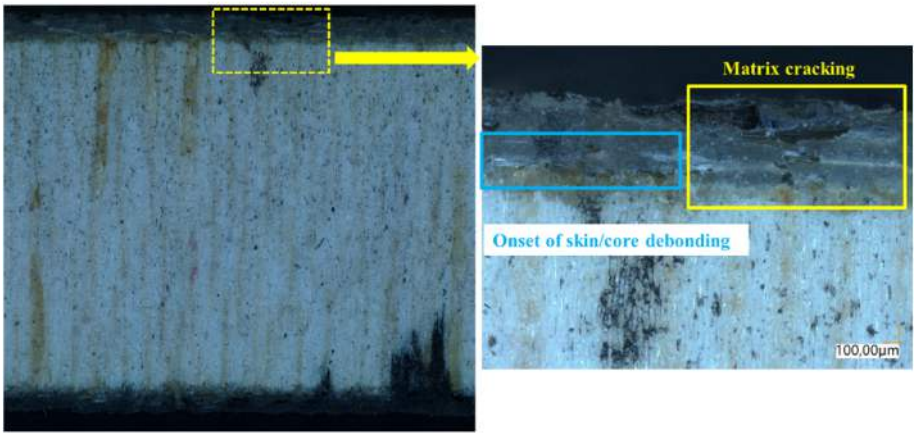

(b) Skin/core damaged surfaces of specimen 5

Fig. 22. Skin and core damage images of specimen 5 stopped in stage AB in 4-point bending tests.

6.3.2. Second clustering process on Cluster I: classification of skin/core debonding and different skin damages

6.3.2.1. Skin damage initiation identification based on cumulative counts. For the skin damage identification, Fig. 26. (a) compares the cumulative counts from skin damages of specimen 5 in stopped tests to those of Cluster I of specimen 1 in non-stopped tests. Fig. 26. (b) compares the cumulative counts from skin damages of specimen 6 in stopped tests to those of Cluster I of specimen 2 in non-stopped tests. Considering the microscope images, in stage AB in Fig. 26. (a), the predominant damages of specimen 5 should be matrix cracking in Cluster 1. In stage BC in Fig. 26. (b), fiber/matrix debonding in Cluster 1 and skin/core debonding in Cluster 4 become more important in specimen 6.

6.3.2.2. Classification of skin/core debonding and different skin damages. To validate the clustering of different skin damage mechanisms in stopped tests, based on the characteristics of the four clustering groups of specimens 1 and 2 in non-stopped tests using non-supervised method, Supervised Pattern Recognition (SPR) method [35] using K-nearest Neighbor (K-NNC) was chosen to discover if AE features of specimens 1 and 2 also exist in specimens 5 and 6. SPR algorithm was trained and tested firstly by the clustering results of specimens 1 and 2 with satisfactory error margins, and then it was applied to specimens 5 and 6. Finally, three clusters have been obtained by the trained SPR algorithm, as shown in Table 6, Fig. 27 and Fig. 28.

It can be seen that the amplitude, duration and peak frequency distributions of specimens 5 and 6 are consistent with those of specimens 1 and 2 in Table 4. For specimen 5, Cluster 1 is predominant, very few signals from Cluster 2 and 4 appear in this stage, and there is no signal from Cluster 3. For specimen 6, the proportions of Cluster 1 and Cluster 4 have increased more in stage BC, and there is no signal from Cluster 3. It demonstrates that matrix cracking and fiber/matrix debonding are

(a) Upper skin damages of specimen 6

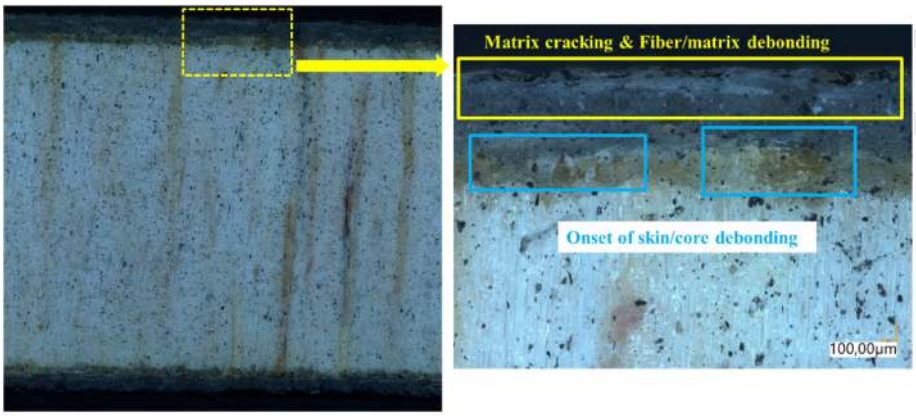

(b) Skin/core damaged surfaces of specimen 6

Fig. 23. Skin and core damage images of specimen 6 stopped in stage BC in 4-point bending tests.

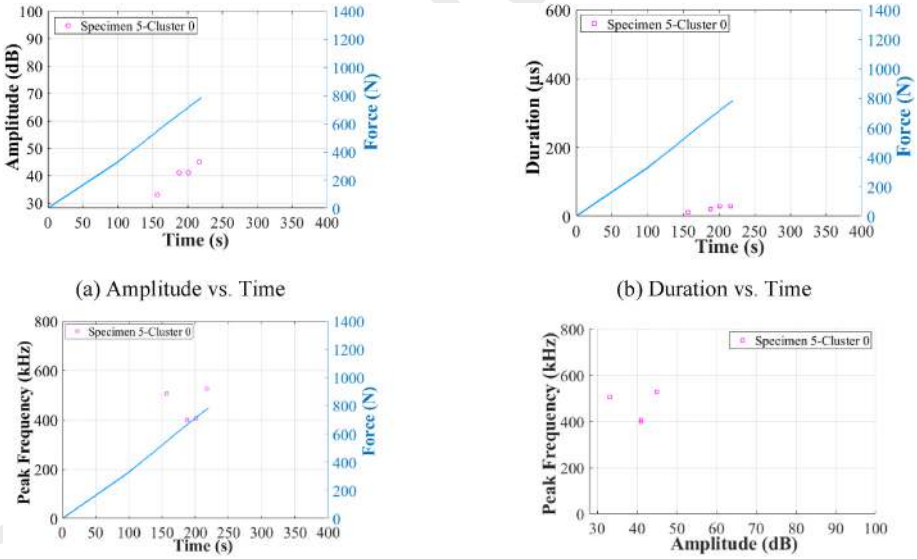

(a) Amplitude vs. Time

(b) Duration vs. Time

(c) Peak frequency vs. Time

(d) Peak frequency vs. Amplitude

Fig. 24. AE parameters of specimen 5 stopped in stage AB in 4-point bending tests.

predominant before the final fracture moment, which also match well with microscope observations in Figs. 23–25. Although skin/core debonding is not obvious in microscope images before the final failure moment, AE sensors are sensitive to the onset of skin/core debonding and can receive the corresponding signals with peak frequency mainly between 200 kHz and 400 kHz.

7. Conclusions

The main conclusions in this study on GFRP-balsa sandwich can be summed as following:

1. Damage modes of GFRP-balsa sandwich under 4-point bending has been identified as: 1) in balsa core: balsa/balsa interfacial debonding between balsa blocks and microcracking in the core; 2) at composite

Table 6
Dominance of different damage mechanisms in stopped 4-point bending tests.

Specimen	Total	Cluster 0	Cluster 1	Cluster 2	Cluster 3	Cluster 4
		Microscopic balsa core cracks & Interfacial debonding	Matrix cracking & Fiber/matrix debonding	Skin delamination	Fiber breakage	Skin/core debonding
5 (Stopped in stage AB)	%:100	25	56	6.5	0	12.5
	Hits:16	4	9	1	0	2
6 (Stopped in stage BC)	%:100	6.8	52.5	4.2	0	36.5
	Hits:118	8	62	5	0	43

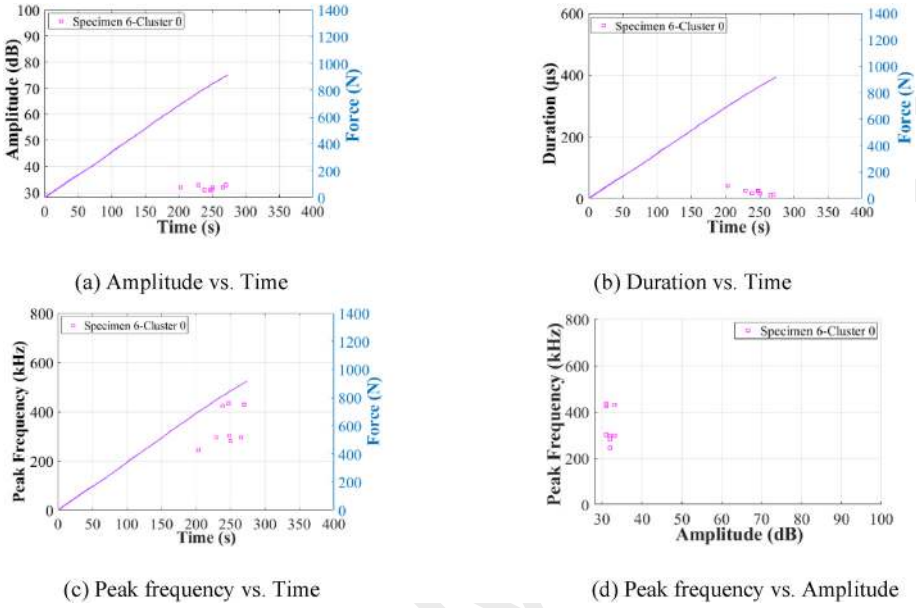

Fig. 25. AE parameters of specimen 6 stopped in stage BC in 4-point bending tests.

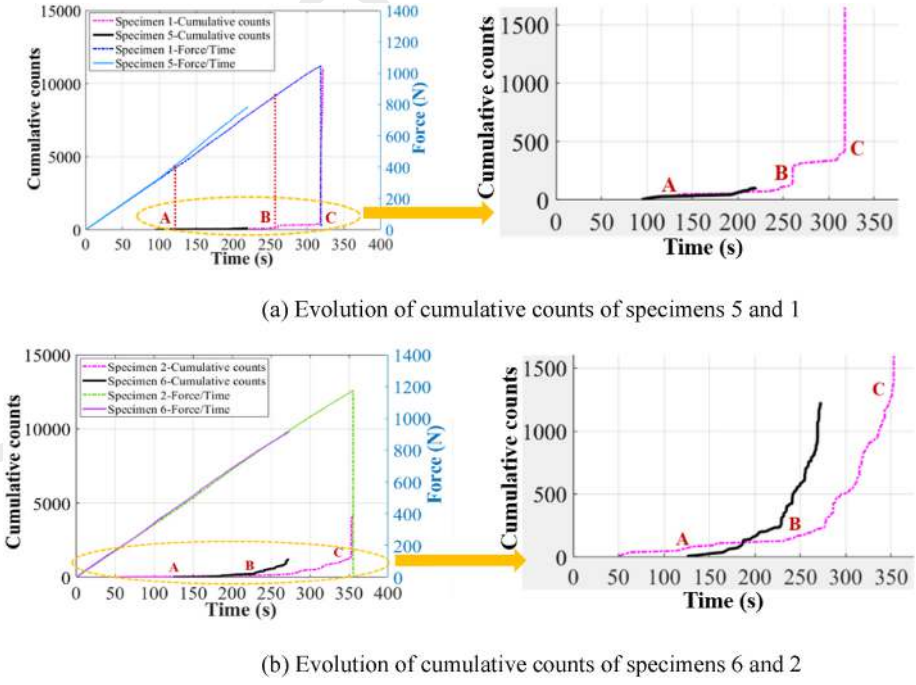

Fig. 26. Cumulative counts vs. time of GFRP-balsa sandwiches in stopped and non-stopped tests.

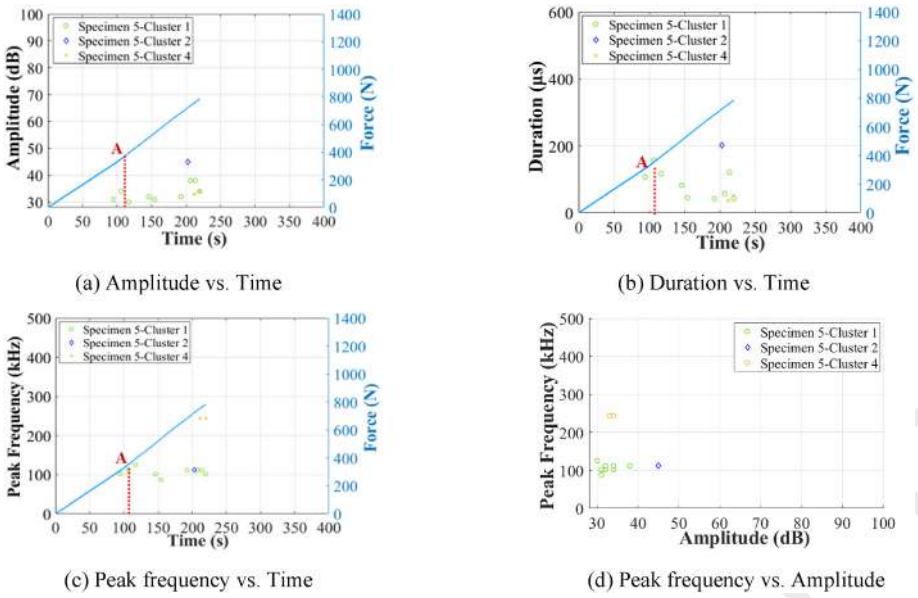

Fig. 27. Clustering results of AE parameters of specimen 5 stopped in stage AB in 4-point bending tests.

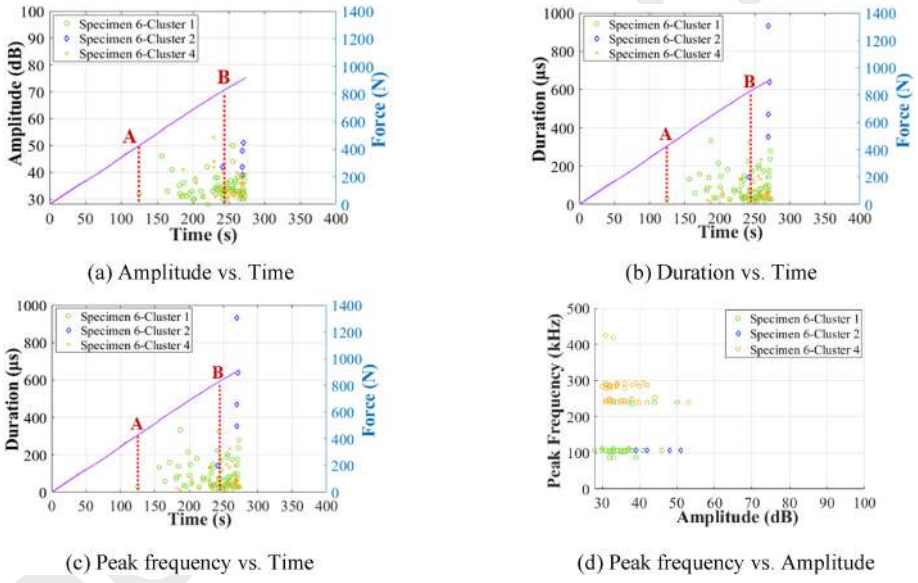

Fig. 28. AE parameters of specimen 6 stopped in stage BC in 4-point bending tests.

skin/core interface: skin/core debonding; 3) in upper composite skin (compressive side): matrix cracking, fiber/matrix debonding, delamination and fiber breakage. Among them, the four skin damage mechanisms are predominant.

2. AE characteristics of GFRP-balsa sandwich have been identified by coupling amplitude, duration and peak frequency distributions (Table 4) of acoustic waveforms. Microscopic balsa core damages show highest peak frequency, shortest duration and low amplitude. Skin/core debonding show higher peak frequency, shorter duration and low amplitude. Matrix cracking and fiber/matrix debonding have the low peak frequency, longer duration and low amplitude. Skin delamination has low peak frequency, longer duration and intermediate amplitude. Fiber breakage has low peak frequency, longest duration and highest amplitude.
3. Cumulative counts have been proven to be very useful for the identification of the initiation of microscopic and macroscopic composite skin damages, showing three obvious transition points corresponding to the beginning of matrix cracking, fiber/matrix debonding and fiber breakage of GFRP laminate skin.
4. Stopped 4-point bending tests have been conducted to validate the proposed damage characterisation approach by two-step clustering process in AE analysis. It demonstrates that matrix cracking is predominant at the lower loading level, the fractions of fiber/matrix debonding and skin/core debonding have increased in the stage just before the final fracture of the specimen.

Concerning the methodology to monitor the damage process in a heterogeneous GFRP-balsa sandwich structure by AE technique, a two-step clustering process coupling the three most relevant AE

parameters (amplitude, peak frequency and duration) has been proposed and validated to classify more than four damage modes of GFRP-balsa sandwich structures under 4-point bending. The results obtained by the proposed method seem convincing and promising for a better understanding of AE analysis in composite sandwich structures in the future. It should be applicable to a structure which is composed of two materials with very different properties such as other balsa composite sandwich, foam sandwich and honeycomb sandwich. But further experimental data is needed to demonstrate the efficacy of this proposed new method.

Declaration of competing interest

The authors declare that they have no known competing financial interests or personal relationships that could have appeared to influence the work reported in this paper.

Data availability

Data will be made available on request.

Acknowledgements

The author Yuan Wu was supported by the China Scholarship Council for 3 years study at the University of Toulouse.

References

[1] Cantwell WJ, Broster G, Davies P. The influence of water immersion on skin-core debonding in GFRP-balsa sandwich structures. J Reinforc Plast Compos 1996;15 (11):1161–72.
[2] Mohammadi MS, Nairn JA. Balsa sandwich composite fracture study: comparison of laminated to solid balsa core materials and debonding from thick balsa core materials. Compos B Eng 2017;122:165–72.
[3] Borrega M, Gibson LJ. Mechanics of balsa (Ochroma pyramidale) wood. Mech Mater 2015;84:75–90.
[4] Legrand V, TranVan L, Jacquemin F, Casari P. Moisture-uptake induced internal stresses in balsa core sandwich composite plate: modeling and experimental. Compos Struct 2015;119:355–64.
[5] Daniel IM, Gdoutos EE, Wang KA, Abot JL. Failure modes of composite sandwich beams. Int J Damage Mech 2002;11(4):309–34.
[6] Zaharia SM, Morariu CO, Nedelcu A, Pop MA. Experimental study of static and fatigue behavior of CFRP-balsa sandwiches under three-point flexural loading. Bioresources 2017;12(2):2673–89.
[7] Sayahlatifi S, Rahimi G, Bokaei A. Experimental and numerical investigation of sandwich structures with balsa core and hybrid corrugated composite/balsa core under three-point bending using digital image correlation. J Sandw Struct Mater 2021;23(1):94–131.
[8] Shi H, Liu W, Fang H. Damage characteristics analysis of GFRP-Balsa sandwich beams under Four-point fatigue bending. Compos Appl Sci Manuf 2018;109: 564–77.
[9] Ammar IB, Karra C, El Mahi A, El Guerjoumaa R, Haddarb M. Mechanical behavior and acoustic emission technique for detecting damage in sandwich structures. Appl Acoust 2014;86:106–17.
[10] Munoz V, Valès B, Perrin M, Pastor ML, Welemane H, Cantarel A, Karama M. Damage detection in CFRP by coupling acoustic emission and infrared thermography. Compos B Eng 2016;85:68–75.
[11] Saeedifar M, Zarouchas D. Damage characterization of laminated composites using acoustic emission: a review. Compos B Eng 2020:108039.
[12] Masmoudi S, El Mahi A, Turki S. Use of piezoelectric as acoustic emission sensor for in situ monitoring of composite structures. Compos B Eng 2015;80:307–20.
[13] Fotouhi M, Saeedifar M, Sadeghi S, Najafabadi MA, Minak G. Investigation of the damage mechanisms for mode I delamination growth in foam core sandwich composites using acoustic emission. Struct Health Monit 2015;14(3):265–80.
[14] McCrory JP, Al-Jumaili SK, Crivelli D, Pearson MR, Eatona M, Featherston CA, Guagliano M, Holford KM, Pullin R. Damage classification in carbon fiber composites using acoustic emission: a comparison of three techniques. Compos B Eng 2015;68:424–30.
[15] Saeedifar M, Najafabadi MA, Zarouchas D, Toudeshky HH, Jalalvandd M. Clustering of interlaminar and intralaminar damages in laminated composites under indentation loading using Acoustic Emission. Compos B Eng 2018;144:206–19.
[16] Abdulaziz AH, Hedaya M, Elsabbagh A, Holford KM, McCrory JP. Acoustic emission source location in composite-honeycomb sandwich panel. Int J Renew Energy Resour 2021;11(2):851–60.
[17] Sikdar S, Ostachowicz W, Pal J. Damage-induced acoustic emission source identification in an advanced sandwich composite structure. Compos Struct 2018;202: 860–6.
[18] Behnia A, Chai HK, Shiotani T. Advanced structural health monitoring of concrete structures with the aid of acoustic emission. Construct Build Mater 2014;65: 282–302.
[19] Barile C, Casavola C, Pappalettera G, Kannan VP. Interpreting the Lempel–Ziv complexity of acoustic emission signals for identifying damage modes in composite materials. Struct Health Monit 2022:14759217221112831.
[20] Barile C, Casavola C, Pappalettera G, Kannan VP. Application of different acoustic emission descriptors in damage assessment of fiber reinforced plastics: a comprehensive review. Eng Fract Mech 2020;235:107083.
[21] De Rosa IM, Santulli C, Sarasini F. Acoustic emission for monitoring the mechanical behaviour of natural fibre composites: a literature review. Compos Appl Sci Manuf 2009;40(9):1456–69.
[22] Oz FE, Ersoy N, Lomov SV. Do high frequency acoustic emission events always represent fiber failure in CFRP laminates. Compos Appl Sci Manuf 2017;103: 230–5.
[23] Friedrich L, Colpo A, Maggi A, Becker T, Lacidogna G, , et allturrioz I. Damage process in glass fiber reinforced polymer specimens using acoustic emission technique with low frequency acquisition. Compos Struct 2021;256:113105.
[24] Barile C, Casavola C, Pappalettera G, Kannan VP. Laplacian score and K-means data clustering for damage characterization of adhesively bonded CFRP composites by means of acoustic emission technique. Appl Acoust 2022;185:108425.
[25] Burud N, Kishen JMC. Damage detection using wavelet entropy of acoustic emission waveforms in concrete under flexure. Struct Health Monit 2021;20(5): 2461–75.
[26] Zhang Y, Zhou B, Yu F, Chen C. Cluster analysis of acoustic emission signals and infrared thermography for defect evolution analysis of glass/epoxy composites. Infrared Phys Technol 2021;112:103581.
[27] Quispitupa A, Shafiq B, Just F, Serrano D. Acoustic emission based tensile characteristics of sandwich composites. Compos B Eng 2004;35(6–8):563–71.
[28] Pashmforoush F, Khamedi R, Fotouhi M, Hajikhani M, Ahmadi M. Damage classification of sandwich composites using acoustic emission technique and k-means genetic algorithm. J Nondestr Eval 2014;33(4):481–92.
[29] Tabrizi IE, Oz FE, Zanjani JSM, Mandal SK, Yildiz M. Failure sequence determination in sandwich structures using concurrent acoustic emission monitoring and postmortem thermography. Mech Mater 2022;164:104113.
[30] Assarar M, Bentahar M, El Mahi A, El Guerjouma R. Monitoring of damage mechanisms in sandwich composite materials using acoustic emission. Int J Damage Mech 2015;24(6):787–804.
[31] Alila F, Fajoui J, Kchaou M, Casari P, Wali N, Gerard R. Mechanical characterization of sandwich composite structure using a new experimental approach. Adv Compos Lett 2016;25(5):096369351602500502.
[32] Wu Y, Pastor ML, Perrin M, Casari P, Gong X. A new methodology to predict moisture effects on mechanical behaviors of GFRP-balsa sandwich by acoustic emission and infrared thermography. Compos Struct 2022;287:115342.
[33] Wu Y, Perrin M, Pastor ML, Casari P, Gong X. On the determination of acoustic emission wave propagation velocity in composite sandwich structures. Compos Struct 2021;259:113231.
[34] Perrin M, Yahyaoui I, Gong X. Acoustic monitoring of timber structures: influence of wood species under bending loading. Construct Build Mater 2019;208:125–34.
[35] Momon S, Godin N, Reynaud P, R'Mili M, Fantozzi G. Unsupervised and supervised classification of AE data collected during fatigue test on CMC at high temperature. Compos Appl Sci Manuf 2012;43(2):254–60.
[36] Sause MGR, Gribov A, Unwin AR, Horn S. Pattern recognition approach to identify natural clusters of acoustic emission signals. Pattern Recogn Lett 2012;33(1): 17–23.
[37] Boussetta H, Beyaoui M, Laksimi A, Walha L, Haddar M. Study of the filament wound glass/polyester composite damage behavior by acoustic emission data unsupervised learning. Appl Acoust 2017;127:175–83.
[38] Li L, Lomov SV, Yan X, Carvelli V. Cluster analysis of acoustic emission signals for 2D and 3D woven glass/epoxy composites. Compos Struct 2014;116:286–99.
[39] Zhou W, Zhao W, Zhang Y, Ding Z. Cluster analysis of acoustic emission signals and deformation measurement for delaminated glass fiber epoxy composites. Compos Struct 2018;195:349–58.
[40] Oskouei AR, Zucchelli A, Ahmadi M, Minak G. An integrated approach based on acoustic emission and mechanical information to evaluate the delamination fracture toughness at mode I in composite laminate. Mater Des 2011;32(3):1444–55.
[41] Andrew JJ, Arumugam V, Bull DJ, Dhakal HN. Residual strength and damage characterization of repaired glass/epoxy composite laminates using AE and DIC. Compos Struct 2016;152:124–39.